Available online at www.sciencedirect.com
ScienceDirect
Acta Materialia 58 (2010) 709–715
Acta MATERIALIA
www.elsevier.com/locate/actamat

Structural properties of materials created through freeze casting

Stephen A. Barr [a], Erik Luijten [b,c,*]

[a] Department of Materials Science and Engineering, University of Illinois at Urbana-Champaign, Urbana, IL 61801, USA
[b] Department of Materials Science and Engineering, Northwestern University, Evanston, IL 60208, USA
[c] Department of Engineering Sciences and Applied Mathematics, Northwestern University, Evanston, IL 60208, USA

Received 24 May 2009; received in revised form 21 September 2009; accepted 23 September 2009
Available online 30 October 2009

Abstract

Upon freezing of an aqueous suspension of colloidal particles, ice platelets or dendrites with high aspect ratios are formed that engulf or reject the particles, depending on their size and the velocity of the advancing ice front. As the particles are pushed between the growing crystals, concentrated regions of colloidal particles are formed. Recent experiments have exploited this to create strong, porous materials with a well-controlled microstructure. We investigate this process by means of molecular dynamics simulations, focusing on the effect of the ice front velocity on the structure of the resulting material. We develop a model that accounts for particle engulfment or rejection by the ice front, and study both columnar and lamellar geometries. The degree of order of the resulting solid and the thickness of the walls surrounding the pores are shown to be determined by front velocity and initial particle concentration in the suspension.

Keywords: Directional solidification; Layered structures; Porous material; Molecular dynamics simulations; Freeze casting

1. Introduction

Strong, lightweight, porous materials are desirable for a wide range of applications, including filters, fuel cells and biomedical implants. One method to create such materials is freeze casting, in which an aqueous suspension of solid particles is cast into a mold and subsequently frozen. The growing ice crystals generate ice fronts that concentrate the suspended particles in the intervening space. Upon removal of the ice through freeze drying, a porous, solid structure remains that can be sintered [1]. Although historically freeze casting has mostly been known for its flexibility and low cost, yielding materials with irregular structure [2], the use of directional freezing [3] permits remarkable control over the resulting pore structure. Indeed, this approach has been used to create a variety of structures, such as silica fiber bundles [3], tubular supports with radially aligned pores [4] and micro-honeycombs [5]. Freeze casting primarily employs suspensions of ceramic particles, but recently it also has been used to fabricate titanium foams with aligned, elongated pores [6]. The field received renewed attention with the work of Deville et al. [7,8], who demonstrated that complex composites can be built with lamellar microstructures that depend on the velocity of the freezing ice front and the initial conditions of the aqueous suspension. The porous scaffold obtained through freeze casting is backfilled with a second phase, resulting in a nacre-like material [7,9].

Whereas various aspects of the freeze-casting process, such as control over spacing between ice platelets [7,8] and the interactions between an advancing ice front and colloidal particles [10,11], have been explored previously, little is known about the arrangement of colloidal particles within the resulting structures. It is therefore the purpose of the present study to investigate by means of molecular dynamics simulations how details of the freezing process affect the resulting solid structure. In particular, we examine the role of ice front velocity and particle concentration. The simulations are restricted to an idealized model system, but we believe that these simulations nevertheless provide guidance for the creation of specific target structures.

* Corresponding author. Address: Department of Materials Science and Engineering, Northwestern University, Evanston, IL 60208, USA. Tel.: +1 847 491 4097; fax: +1 847 491 7820.
E-mail address: luijten@northwestern.edu (E. Luijten).

1359-6454/$36.00
doi:10.1016/j.actamat.2009.09.050

2. Model and method

We perform molecular dynamics simulations using a custom-modified version of the LAMMPS package [12]. To reproduce both the lamellar structure resulting from platelet-like ice crystals [7] and the honeycomb structures observed in Refs. [3,5], we employ three-dimensional simulations in a planar and a columnar geometry. In the lamellar system, depicted schematically in Fig. 1, two parallel ice fronts (lateral area $10\,\mu m \times 10\,\mu m$) are placed initially 10 μm apart. As the platelets become thicker, these ice fronts advance towards each other (along the z-axis) at a constant velocity until they meet. In this case, we employ periodic boundary conditions in the x and y directions. The columnar geometry is generated by modeling the dendrites as rods that are arranged in a 2×2 hexagonal cell (Fig. 2). The rods are aligned along the z direction, with a nearest-neighbor spacing of 5 μm. During the simulation, their radius increases at a constant rate from 0 to 2.5 μm. The cell has a height of 10 μm, and to minimize finite-size effects we replicate it periodically in all three dimensions, creating an infinite array of infinitely long dendrites.

In both geometries, the suspended particles are modeled as monodisperse spheres that interact through a purely repulsive potential:

$$V(r) = k_B T \left(\frac{\sigma}{r}\right)^{48}, \tag{1}$$

where $\sigma = 200$ nm is the diameter of the particles, k_B is Boltzmann's constant, and the temperature is set to $T = 0\,^{\circ}C$. The potential is cut off at $r = 1.2\sigma$. The power law is chosen to create an excluded-volume interaction that is steep enough to avoid unphysical particle overlaps at high concentrations, while simultaneously permitting a time step that is not too small. Its specific value does not affect the outcome of our calculations. All simulations

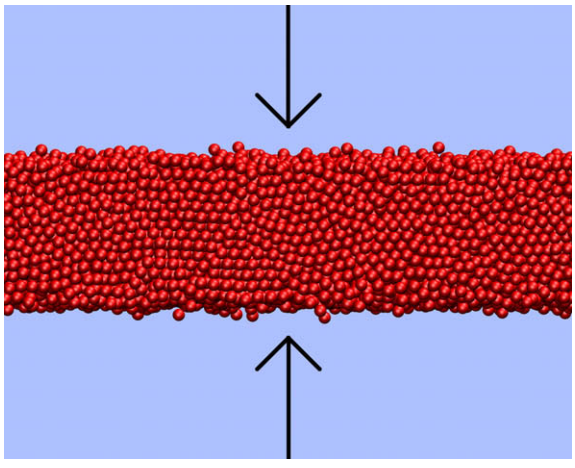

Fig. 1. Schematic diagram of the lamellar geometry. The two planar ice fronts advance at a constant rate in the direction of the arrows, which run parallel to the z-axis. The fronts represent growing platelets that concentrate the suspended colloidal particles in the center region. All simulations are performed in three dimensions.

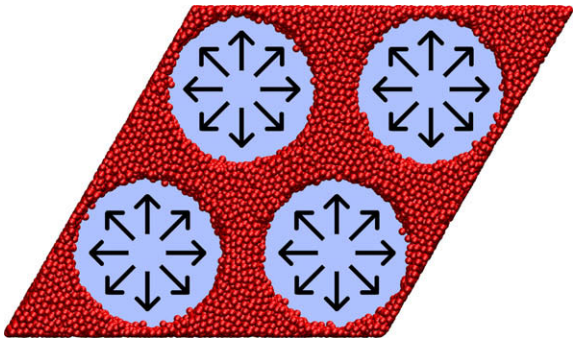

Fig. 2. Schematic representation of the columnar geometry, looking down the z-axis. Cylindrical dendrites of ice form parallel to the z-axis and grow radially outward at a constant rate. As in Fig. 1, the solid particles are pushed into the intervening regions.

are carried out in the NVT ensemble and the temperature is controlled by means of a Langevin thermostat. Initially, the particles are distributed homogeneously throughout the simulation cell and brought to thermal equilibrium. The interaction between the particles and the ice front is represented by the van der Waals potential for a sphere and a plane near contact [13]:

$$W(h) = -\frac{AR}{6h}, \tag{2}$$

where $R = \sigma/2$ is the particle radius, A the Hamaker constant and h the surface-to-surface distance between the ice front and the particle. For alumina particles (used in Ref. [7]) pushed by ice, $A = -2 \times 10^{-21}$ J, as calculated using the Lifshitz theory [14]. Its negative value indicates a repulsive interaction [15,16]. Our choice of $\sigma = 200$ nm is comparable to the diameter of particles used in various experiments [2,7,8]. In order to relate our findings to recent experiments that employed titanium particles [6], we also investigate systems with $\sigma = 20\,\mu m$. In this case $A = -7 \times 10^{-20}$ J [17]. For these large particles we only consider a columnar geometry, in which the dendrites have a nearest-neighbor spacing of 800 μm and the height of the simulation cell equals 1600 μm.

The repulsive interaction between the advancing ice front and the suspended particles causes the latter to be pushed into the interlamellar or interdendritic space, provided the front velocity, v_f, is less than the critical velocity, v_c. Once the front velocity exceeds this critical value, $v_f > v_c$, particles are engulfed by the ice front [6,8,16]. Particle engulfment has a twofold effect on the porous structures that are created during freeze casting: (i) it reduces the particle concentration in the space between the approaching ice fronts, allowing the growth of larger ice crystals, and hence larger pores and (ii) the particles that are incorporated *within* the ice crystals can form narrow "linkers" of touching particles that, upon freeze drying, act as interconnects within the porous material. Such linkers have been observed in the lamellar structures formed by platelet-shaped ice crystals [7]. We incorporate this phenomenon in the molecular dynamics simulations by setting

a distance δ, such that a particle is engulfed if its surface-to-surface distance to the ice front, h, is less than δ. Once engulfed, the particle remains stationary for the duration of the simulation. The distance δ is chosen such that the repulsive force exerted on the particle by the ice front equals the viscous drag force on the particle at the critical velocity, v_c. For alumina particles of diameter 200 nm pushed by ice in water, $v_c = 125\ \mu m\ s^{-1}$ [16,6]. The drag force F_d is calculated from Stokes' law:

$$F_d = 6\pi\eta R v_c, \tag{3}$$

where $\eta = 1.8$ cP is the viscosity of water at $T = 0\ ^\circ C$. By setting the frictional force used in the Langevin thermostat to correspond to the solvent viscosity, we arrive at a simulation method that takes into account particle engulfment. This method ignores the effect of gravity, the curvature of the ice front and the influence the particles have on the shape of the ice front. While other simulation studies have used more detailed models of the interactions between a particle and an advancing solidification front [10,11], these have focused on a single colloidal particle. In contrast, our simplified model allows us to consider realistic particle concentrations and front velocities while capturing the important aspects of the engulfment process, including the collective behavior of large numbers of particles. Our simulations involve 35 000–280 000 particles and took up to 1600 CPU h per run. In total, 51 runs were performed to cover all parameter choices, requiring 4 months of CPU time on a quad-core Intel Xeon E5472 processor.

3. Results

3.1. Evolution of colloidal volume fraction upon ice crystal growth

We first present the results for particles with a diameter of 200 nm. To determine the effect of front velocity, we investigate six different values of v_f, namely 2, 20, 40, 60, 80 and 100 $\mu m\ s^{-1}$. These values span the range of experimentally achievable front velocities [7]. We also investigate the role of colloid concentration by considering three different values of the initial volume fraction, $\phi_i = 0.15$, 0.25 and 0.35. It is worth noting that the front velocity plays a role in determining whether the ice crystals form as platelets or dendrites [8]. However, in our calculations we have treated front velocity and geometry as independent parameters.

As the platelets or dendrites grow, the volume accessible to the particles decreases. At the same time some of the particles become engulfed, reducing the number of free particles in the system. Particles can be engulfed even if $v_f < v_c$ if particles have a sufficiently high velocity towards the ice front or if they are surrounded by other particles which force them into the ice front [18]. Because of this, the volume fraction of particles in the aqueous phase, ϕ, changes as the ice crystals grow. As an example, this is illustrated for a lamellar geometry in Fig. 3, which shows ϕ as a function of the distance d each of the ice fronts has traveled. We also indicate the corresponding width of the gap between the ice fronts, $\Delta = 10\ \mu m - 2d$. Most of the particles are pushed, with only a small fraction being engulfed, and ϕ increases monotonically. This behavior continues until a volume fraction $\phi \approx 0.65$ is reached, i.e. close to the random close-packed volume fraction. For $\phi_i = 0.15$ and $v_f = 2\ \mu m\ s^{-1}$ this occurs at $d = 19.5\sigma$, or a gap width $\Delta = 2.2\ \mu m$. At this point, the colloidal particles form a solid which prevents the particles closest to the ice front from being pushed farther. For higher front velocities, this point occurs at larger values of d (thicker platelets) since more particles are engulfed before a solid is formed and a smaller gap volume is required to reach the same volume fraction. After this, the ice front moves through the solid, pushing the remaining particles only over short distances, typically a fraction of their diameter σ, before engulfing them. Interestingly, the lowest front velocity, $v_f = 2\ \mu m\ s^{-1}$, does not result in the largest final volume fraction. This can be understood as follows. As the system approaches solid-like densities, the pressure becomes large enough to force the particles into the ice front. At the lowest front velocity, more time is spent in this state and consequently more particles are engulfed. This, however, is not a large effect and the difference in volume fraction between $v_f = 2\ \mu m\ s^{-1}$ and $v_f = 20\ \mu m\ s^{-1}$ is less than 0.03.

The behavior for the columnar geometry (Fig. 4) is quite similar, although there is no dependence on front velocity until the random close-packed volume fraction is reached, indicating that there is a lesser tendency of particle engulfment in this geometry.

3.2. Structure of solid phase

Our simulations do not only provide information on the evolution of the system as the ice crystals grow, but also

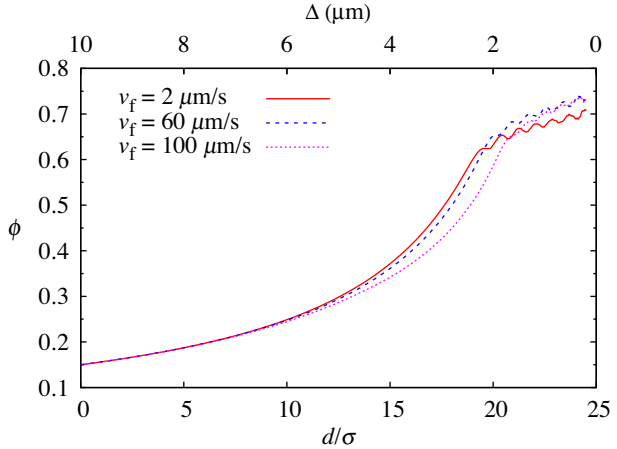

Fig. 3. Volume fraction of colloids in the liquid phase, ϕ, as a function of the distance d each of the approaching ice fronts has traveled, for the lamellar geometry and an initial volume fraction $\phi_i = 0.15$. The top axis shows the width Δ of the gap between the platelets. The volume fraction increases gradually and monotonically until a value of $\phi \approx 0.65$ is reached, at which point the colloids form a solid. As the ice moves through this solid, the volume fraction increases more slowly and the oscillations observed are due to the ice moving through layers of particles, cf. Fig. 6.

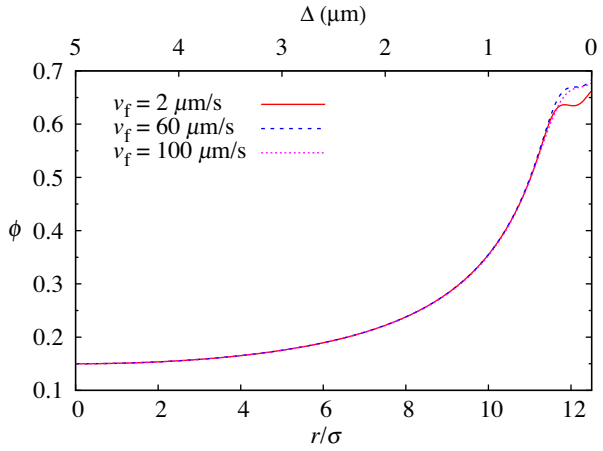

Fig. 4. Volume fraction ϕ of colloids in the liquid phase as a function of the dendrite radius r, for the columnar geometry and an initial volume fraction $\phi_i = 0.15$. The graph also shows the width Δ of the interdendritic space, as measured along the center-to-center axis between neighboring dendrites. The volume fraction increases gradually and monotonically until a value of $\phi \approx 0.65$ is reached, at which point the colloids form a solid. As the ice moves through the solid, ϕ increases more slowly.

permit investigation of the resulting solid colloidal phase. Once the colloids have been compressed into a dense state, the ice front continues to invade this phase, engulfing the colloids. Colloidal rearrangements may still occur at this stage, depending on front velocity. For the lamellar geometry, the freezing process is complete when neighboring ice fronts meet, i.e. at $d = 5$ μm(25σ). For the columnar geometry, this point (i.e. $d = 12.5\sigma = 2.5$ μm) marks the end of isotropic radial growth of the dendrites; the ice will continue to invade the interstitial voids, but we do not observe any further displacement of the colloids. In the experimental system, the ice is subsequently removed through sublimation and loose particles (i.e. those that are disconnected from the solid structure) have to be disregarded. In our simulations, we determine which particles remain by means of a cluster-finding algorithm that identifies groups of connected particles. For this purpose we define two particles as connected if their surfaces are separated by less than 10 nm. Fig. 5 shows the final configurations of the particles which would remain after the ice is removed for $\phi_i = 0.35$ and a range of front velocities. As mentioned, higher front velocities lead to thinner colloidal configurations since more particles are engulfed before a solid is formed. In Ref. [7], some of the engulfed particles were found to form bridges that link neighboring colloidal domains, thus mimicking the inorganic bridges that are found in nacre (cf. also Ref. [9]). Although we did not observe such bridges in our simulations, we found that higher front velocities result in rougher surfaces, since the particles have less time to rearrange as they are being pushed. This effect is more pronounced for higher initial volume fractions. The ability to manipulate the surface roughness is desirable, as it can be exploited to influence the bonding between the colloidal phase and the second

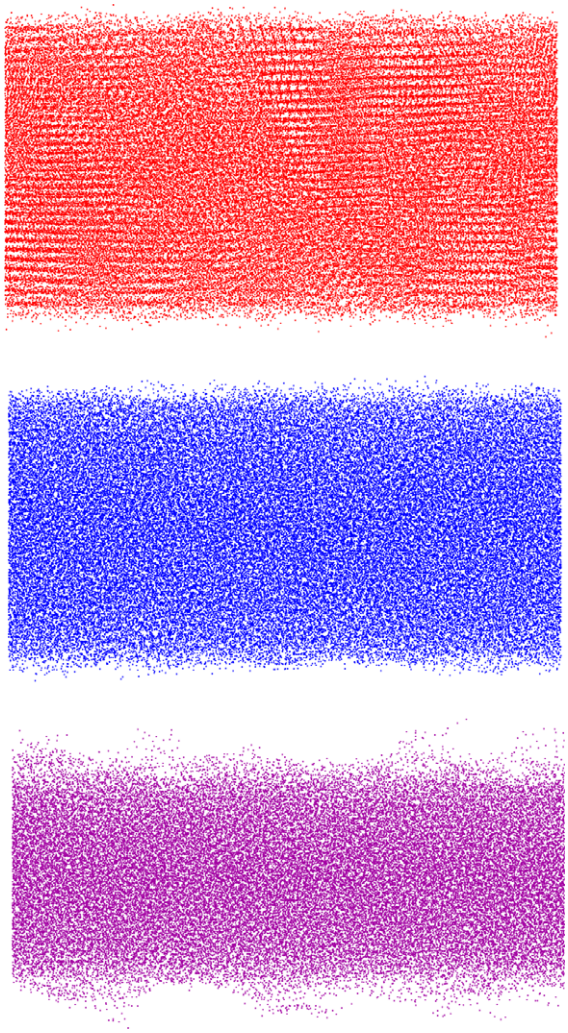

Fig. 5. Final configuration of particles which remain after sublimation for $v_f = 2$ μm s^{-1} (top), $v_f = 40$ μm s^{-1} (middle), and $v_f = 100$ μm s^{-1} (bottom) for an initial volume fraction $\phi_i = 0.35$ in the lamellar geometry. The particles are depicted as points for clarity. Lower front velocities lead to thicker walls since fewer particles are engulfed, and higher front velocities result in rougher surfaces. For $v_f = 2$ μm s^{-1}, layers are clearly visible.

phase that is backfilled into the pores left by the sublimated ice.

Our results for the columnar geometry corroborate the role played by particle engulfment in determining the thickness and surface structure of the colloidal phase. Indeed, since virtually no engulfment is observed in this case (cf. Fig. 4), we observe hardly any difference in wall thickness and surface roughness for different front velocities.

Inspection of the configurations depicted in Fig. 5 suggests that, for low front velocities, the particles form layers that are aligned parallel to the ice front. This observation is confirmed in Fig. 6, which shows the density profile in the direction perpendicular to the ice front, $\rho(z)$, for an initial volume fraction $\phi_i = 0.25$ and three different front velocities. The density profile not only emphasizes the dependence on front velocity, but also shows more pronounced layering near the edges (surfaces) of the dense phase. This

arises because the colloids in the outer layers have been pushed over larger distances prior to being engulfed, allowing the system to arrange into a more regular structure. The question then arises if regular colloidal arrangements can be observed within a layer, at least for the outer layers at the lowest front velocities. To determine this, we probe the two-dimensional pair correlation function $g_{2d}(r)$ within a slab that contains the layer closest to the surface. As can be seen in Fig. 7, there is no long-range order, even when well-defined layers are formed, and the peaks are indicative of a liquid-like arrangement. The front velocity has little effect on the structure within a layer; even though the nearest-neighbor peak is highest for $v_f = 2$ μm s^{-1}, the behavior at larger distances is independent of v_f. We find qualitatively similar results for other layers, and for different initial volume fractions.

In analogy with these observations, we find for the columnar geometry that low front velocities result in the formation of cylindrical shells around the dendrites. This is quantified by means of the radial distribution function of the particles around the dendrites, $g_{d,p}(r)$, as shown in Fig. 8 for $\phi_i = 0.15$. Interestingly, although Fig. 4 shows that virtual no particle engulfment takes place in this geometry and hence the evolution of the colloidal volume fraction is practically independent of front velocity, we find that the structure within the compressed phase varies strongly with front velocity. For $v_f = 100$ μm s^{-1}, a layered structure no longer develops. The intra-layer structure is characterized by means of the two-dimensional pair correlation function calculated within a cylindrical shell containing the first particle layer (corresponding to the leftmost peak in Fig. 8). As with the lamellar geometry, we observe clear peaks, but there is no long-range order (see inset of Fig. 7).

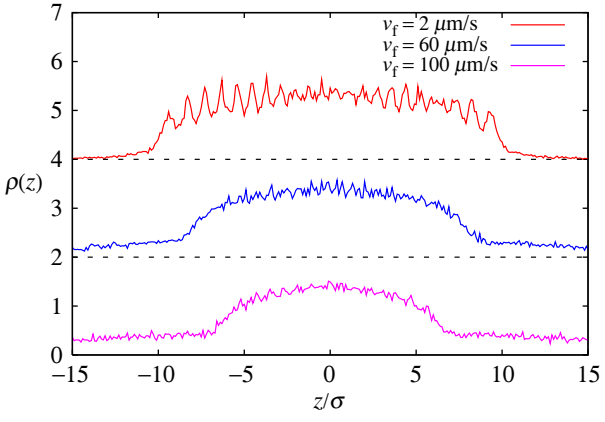

Fig. 6. Density profile $\rho(z)$ of the final configuration of the particles for the lamellar geometry and $\phi_i = 0.25$. Different front velocities are offset for clarity with $v_f = 2$ μm s^{-1} (top), $v_f = 60$ μm s^{-1} (middle), and $v_f = 100$ μm s^{-1} (bottom). For $v_f = 2$ μm s^{-1} there are well-defined layers that are not seen for the higher front velocities. Note that for these higher velocities $\rho(z)$ does not decay to zero outside the center region because of particle engulfment.

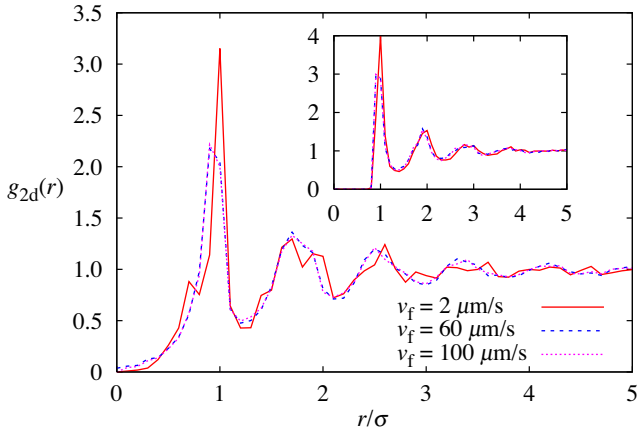

Fig. 7. Two-dimensional pair correlation function $g_{2d}(r)$ for the lamellar geometry, calculated within a planar slab (parallel to the advancing ice front) that contains the particle layer closest to the surface. The initial volume fraction is $\phi_i = 0.25$ and curves for three different front velocities are shown. Even for $v_f = 2$ μm s^{-1}, when well-defined layers form (cf. Fig. 6), no long-range order is observed within a layer. Higher front velocities show similar behavior. The inset shows the same quantity for the columnar geometry. In this case, $g_{2d}(r)$ is calculated within a region bounded by two concentric cylindrical shells around a dendrite, chosen such that the region contains the particle layer closest to the ice front (i.e. the surface layer of the resulting solid structure).

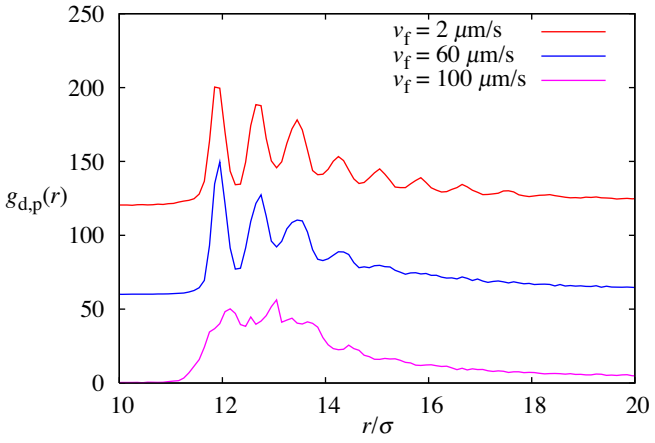

Fig. 8. Radial distribution function $g_{d,p}(r)$ of the particles around the dendrites, for the columnar geometry with an initial volume fraction $\phi_i = 0.15$. Different front velocities are offset for clarity, with $v_f = 2$ μm s^{-1} (top), $v_f = 60$ μm s^{-1} (middle), and $v_f = 100$ μm s^{-1} (bottom). The peaks in $g_{d,p}(r)$ correspond to layers of particles forming concentric cylindrical shells around the dendrites. Lower front velocities result in well-defined layers not observed for the highest front velocity, $v_f = 100$ μm s^{-1}.

3.3. Role of particle size

For both lamellar and columnar geometries, we conclude that layers form for lower front velocities because the particles have enough time to rearrange as they aggregate in front of the advancing ice. This can be confirmed by comparing the diffusive behavior of the particles to the front velocity. Using the drag force computed in Eq. (3),

we obtain a diffusion coefficient $D = 1.11 \times 10^{-12}$ m^2 s^{-1}. Accordingly, a particle will diffuse over a distance equal to its own diameter in 6×10^{-3} s, whereas it takes a front velocity of 33 μm s^{-1} to push the particle over the same distance in the same time. This is indeed consistent with the observation that we see well-ordered layers for $v_f = 2$ μm s^{-1} but not for $v_f = 100$ μm s^{-1}. Although we do not observe a sharp transition from order to disorder, the diffusion coefficient can be used to estimate how slowly the ice front must advance to obtain a layered structure. For example, for much larger particles with $\sigma = 20$ μm (comparable to the coarse titanium powder employed in Ref. [6]), the diffusion coefficient is 100 times smaller at $D = 1.11 \times 10^{-14}$ m^2 s^{-1}. In this case it takes 6000 s for a particle to diffuse over its diameter and an ice front advancing at 3.3×10^{-3} μm s^{-1} would push the particle over the same distance in that time. Because of this slow diffusion rate, particles are unable to rearrange as they are pushed at typical front velocities, and long-range order cannot be achieved. To demonstrate this, we simulate these larger particles in a columnar geometry with a nearest-neighbor spacing between dendrites of 800 μm and measure the radial distribution function $g_{d,p}(r)$ in the final configuration, as shown in Fig. 9 for $v_f = 1$ μm s^{-1} and $\phi_i = 0.15$. There are no well-defined layers and the structure resembles what is observed for $\sigma = 200$ nm at $v_f = 100$ μm s^{-1} (Fig. 8).

The second effect that arises when larger particles are employed is the decrease in critical front velocity, v_c. For 200 nm particles, the front velocities we employ are always less than v_c and thus in all cases only a small fraction of the particles are engulfed before a solid is formed (cf. Figs. 3 and 4). However, for $\sigma = 20$ μm different behavior is observed. The critical front velocity for this system is 37 μm s^{-1} [6] and thus the range of front velocities that

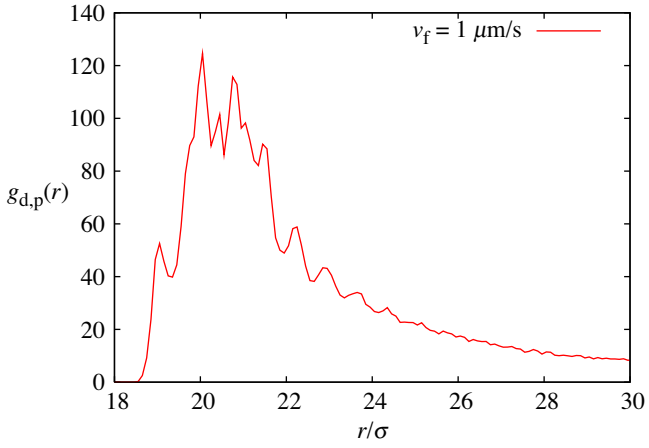

Fig. 9. Radial distribution function $g_{d,p}(r)$ of large particles (diameter $\sigma = 20$ μm, initial volume fraction $\phi_i = 0.15$) around dendrites in a columnar geometry with a nearest-neighbor separation of 800 μm. In this counterpart of Fig. 8 (which pertains to particles with a 100 times smaller diameter), no layers are formed around the dendrites, even at the lowest front velocity of 1 μm s^{-1}.

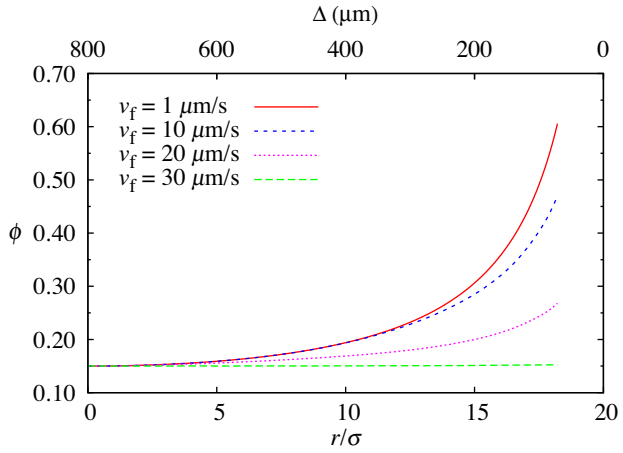

Fig. 10. Volume fraction ϕ of unengulfed particles (diameter $\sigma = 20$ μm) as a function of the dendrite radius r, for the columnar geometry and an initial volume fraction $\phi_i = 0.15$. The top axis shows the width Δ of the interdendritic space. Compared to particles with a smaller diameter (Fig. 4), significant numbers of particles are engulfed, even at front velocities well below the critical front velocity.

results in pushing of particles is diminished. Also, within that range, we find that the front velocity has a larger effect on the final volume fraction of the system. This is illustrated in Fig. 10, which is the counterpart of Fig. 4, showing the instantaneous volume fraction of particles for different values of v_f at a fixed initial volume fraction of $\phi_i = 0.15$. If the front velocity exceeds 30 μm s^{-1}, particles are never pushed and thus remain homogeneously distributed. Front velocities of 10 and 20 μm s^{-1} do result in particles being pushed over long distances and the volume fraction in the interdendritic regions increases; however, many particles are still engulfed and the final volume fractions are not high enough for a solid to form. Only at the lowest front velocity of 1 μm s^{-1} are a sufficient number of particles pushed to form a solid. From this, we see that for large particle sizes the front velocity only affects the fraction of particles that are engulfed, not the structure of the resulting solid phase.

4. Conclusions

Cryochemical methods hold significant promise for the manufacturing of nano- and microscale materials. Motivated by the recent experimental demonstration that freeze casting can be employed to fabricate composite materials with a well-controlled microstructure, we have investigated the effects of ice front velocity, ice crystal shape (lamellar and dendritic), particle concentration, and particle size on the properties of systems undergoing freeze casting. Since our molecular dynamics simulations focus on large-scale structural properties and involve several 100 000 particles, we have employed a simplified model of the engulfment process.

For submicron particles, we find that lower front velocities enable particles to rearrange while they are pushed by

the ice front, resulting in a solid phase that is ordered in the direction of the crystal growth. In addition, the front velocity affects the fraction of particles that is engulfed by the advancing ice front, which in turn controls the thickness of the solid phases that are formed between the ice crystals. For large particles (diameter 20 μm), the front velocity has a much greater effect on the number of particles that are engulfed, even well below the critical front velocity, and low ice front velocities are required to create a solid phase. Furthermore, the diffusivity of these large particles is too small to permit the formation of ordered structures as the ice front advances.

To our knowledge this is the first attempt to employ molecular dynamics simulations for the investigation of a system undergoing freeze casting. Although our approach involves a number of simplifications, such as the assumption of monodisperse particles, the neglect of gravitational effects and the stochastic modeling of the engulfment process, we believe that it may foster insight into the effect of various process variables on the resulting "green body" and serve as a starting point for further simulations. For example, our method could be extended to determine if the freezing of suspensions containing a mixture of colloidal particles of different sizes (such as a binary mixture) can be used to enhance materials properties. Furthermore, the structures obtained in our simulations could be used as input for sintering calculations.

Acknowledgments

We are grateful to David Dunand for bringing this topic to our attention and for helpful comments. This material is based upon work supported by the National Science Foundation under Grant No. DMR-0346914.

Appendix A. Supplementary material

Supplementary data associated with this article can be found, in the online version, at doi:10.1016/j.actamat.2009.09.050.

References

[1] Fukasawa T, Ando M, Ohji T, Kanzaki S. J Am Ceram Soc 2001;84:230.
[2] Sofie SW, Dogan F. J Am Ceram Soc 2001;84:1459.
[3] Mahler W, Bechtold MF. Nature 1980;285:27.
[4] Moon JW, Hwang HJ, Awano M, Maeda K. Mater Lett 2003;57:1428.
[5] Mukai SR, Nishihara H, Tamon H. Chem Commun 2004:874.
[6] Chino Y, Dunand DC. Acta Mater 2008;56:105.
[7] Deville S, Saiz E, Nalla RK, Tomsia AP. Science 2006;311:515.
[8] Deville S, Saiz E, Tomsia AP. Acta Mater 2007;55:1965.
[9] Munch E, Launey ME, Alsem DH, Saiz E, Tomsia AP, Ritchie RO. Science 2008;322:1516.
[10] Garvin JW, Udaykumar HS. J Cryst Growth 2003;252:467.
[11] Garvin JW, Yang Y, Udaykumar HS. Int J Heat Mass Transfer 2007;50:2969.
[12] Plimpton SJ. J Comp Phys 1995;117:1.
[13] Parsegian VA. Van der Waals forces. Cambridge: Cambridge University Press; 2006.
[14] Israelachvili JN. Intermolecular and surface forces. 2nd ed. San Diego (CA): Academic Press; 1992.
[15] Visser J. Adv Colloid Interface Sci 1981;15:157.
[16] Casses P, Azouni-Aidi MA. Adv Colloid Interface Sci 1994;50:103.
[17] Larson I, Drummond CJ, Chan DYC, Grieser F. J Am Chem Soc 1993;115:11885.
[18] Youssef YM, Dashwood RJ, Lee PD. Compos Part A 2005;36:747.